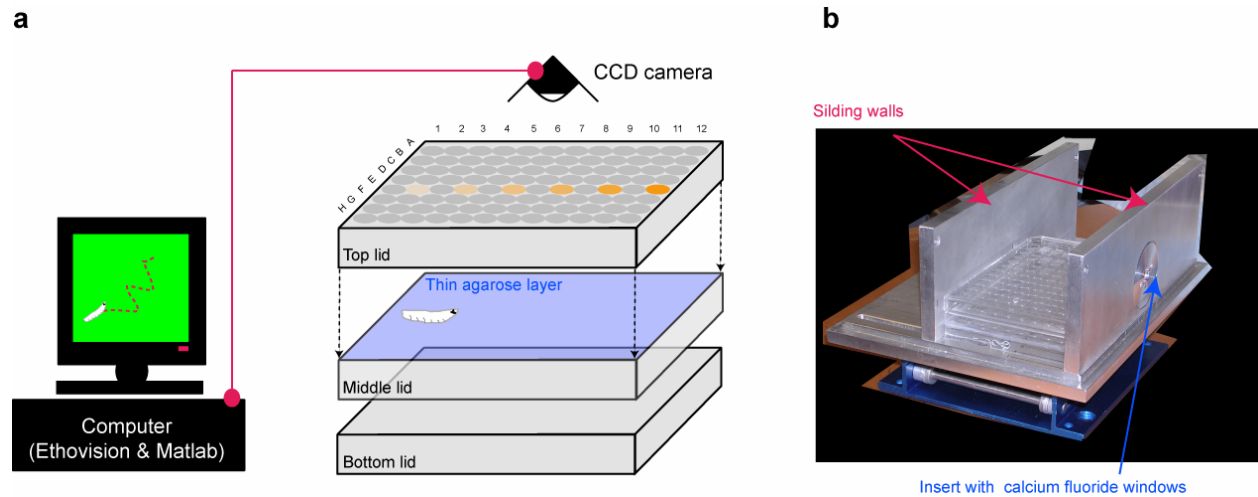# Bilateral olfactory sensory input enhances chemotaxis behavior
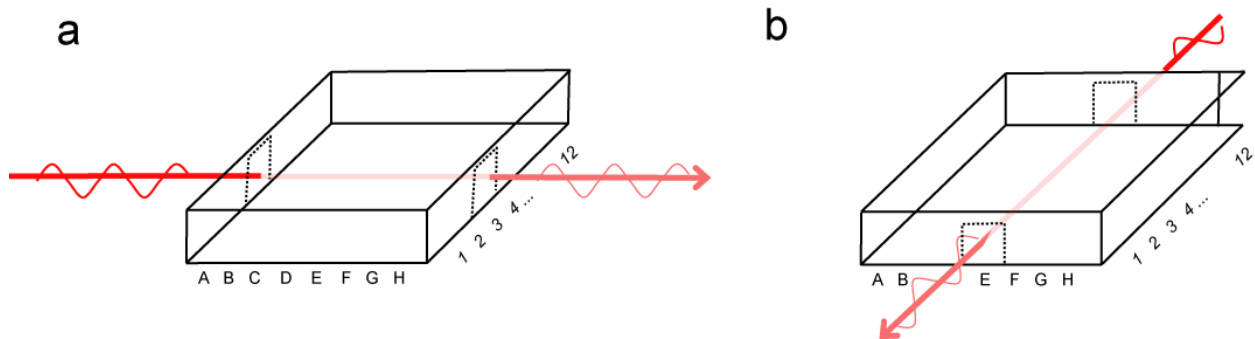
Matthieu Louis, Thomas Huber, Richard Benton, Thomas P. Sakmar, and Leslie B. Vosshall
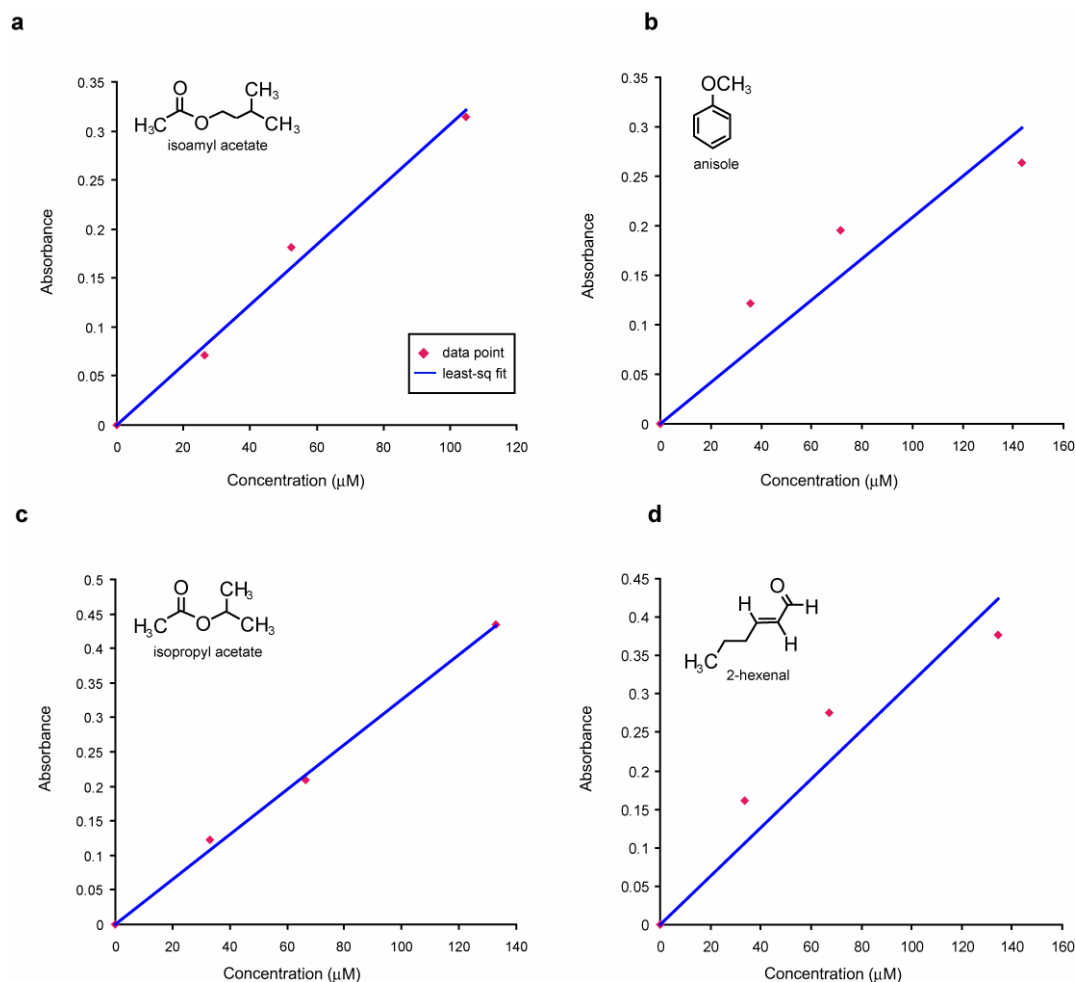
Supplementary Figure 1

a

b

Supplementary Figure 1: Description of the multiple-odor-source device. (a) Schematic illustration of the apparatus. Odor droplets (10 μl) of various concentrations represented by different intensities of orange color are hanging from the inside ceiling of the top lid. **(b)** Photograph of the aluminum box used to enclose the multi-source plate assay for the spectroscopic analysis described in **Fig. 1** and **Supplementary Fig. 2**. The walls of this box can be adjusted to orient the plate lengthwise or widthwise in the beam of the infrared spectrophotometer sample chamber.
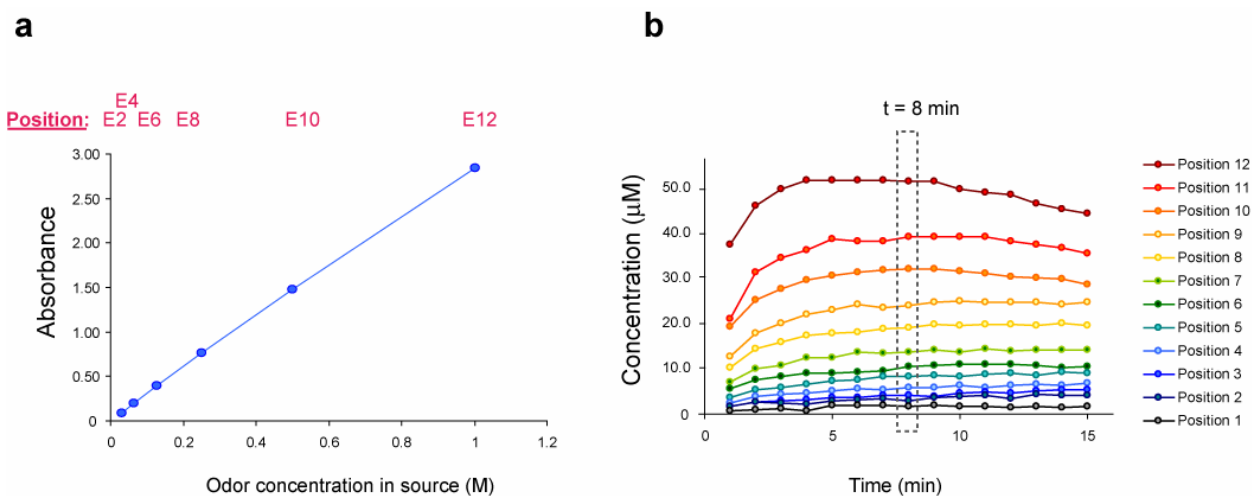
a

b

Supplementary Figure 2: **Procedure followed to determine the odor concentration along sections of the plate assay. (a)** Measurement of the average odor concentration at one particular position of the length of the plate. A square window cut into the lateral walls of the length of the plate permitted us to measure the time-course of the cumulative absorbance, and thereby the average odor concentration, along a given section of the plate. Concentrations were measured at the center of rows 1 to 12. **(b)** Measurement of the average odor concentration at one particular position of the width of the plate. Concentrations were measured at the center of columns A to H.

Supplementary Figure 3: Determination of molar extinction coefficients in gaseous phase by variation of the odor sample concentration. The odor sample was contained in a gas cell with a path length of 10.2 cm. The red diamonds represent the absorbance measured for a given odor concentration. The blue curves result from linear regressions. **(a)** For isoamyl acetate, the three sample concentrations considered were 26.2 μM, 52.4 μM, 104.8 μM. Absorbance was measured at 1764 cm^{-1}. Upon least squares regression ($R^2 = 0.99$), the molar extinction coefficient $\varepsilon^{\text{isoamyl acetate}}$ is estimated to be 310 M^{-1} cm^{-1}. **(b)** For anisole, absorbance was measured at 1254 cm^{-1} and the sample concentrations were 35.8 μM, 71.6 μM, 143.3 μM. Least squares regression ($R^2 = 0.85$) yields $\varepsilon^{\text{anisole}} = 210$ M^{-1} cm^{-1}. **(c)** For isopropyl acetate, absorbance was measured at 1759 cm^{-1} and the sample concentrations used were 33.2 μM, 66.5 μM, 133.0 μM. Least squares regression ($R^2 = 0.99$) yields $\varepsilon^{\text{isopropyl acetate}} = 330$ M^{-1} cm^{-1}. **(d)** For 2-hexenal, absorbance was measured at 1716 cm^{-1} and the sample concentrations used were 33.5 μM, 67.1 μM, 134.2 μM. Least squares regression ($R^2 = 0.88$) yields $\varepsilon^{\text{2-hexenal}} = 320$ M^{-1} cm^{-1}.
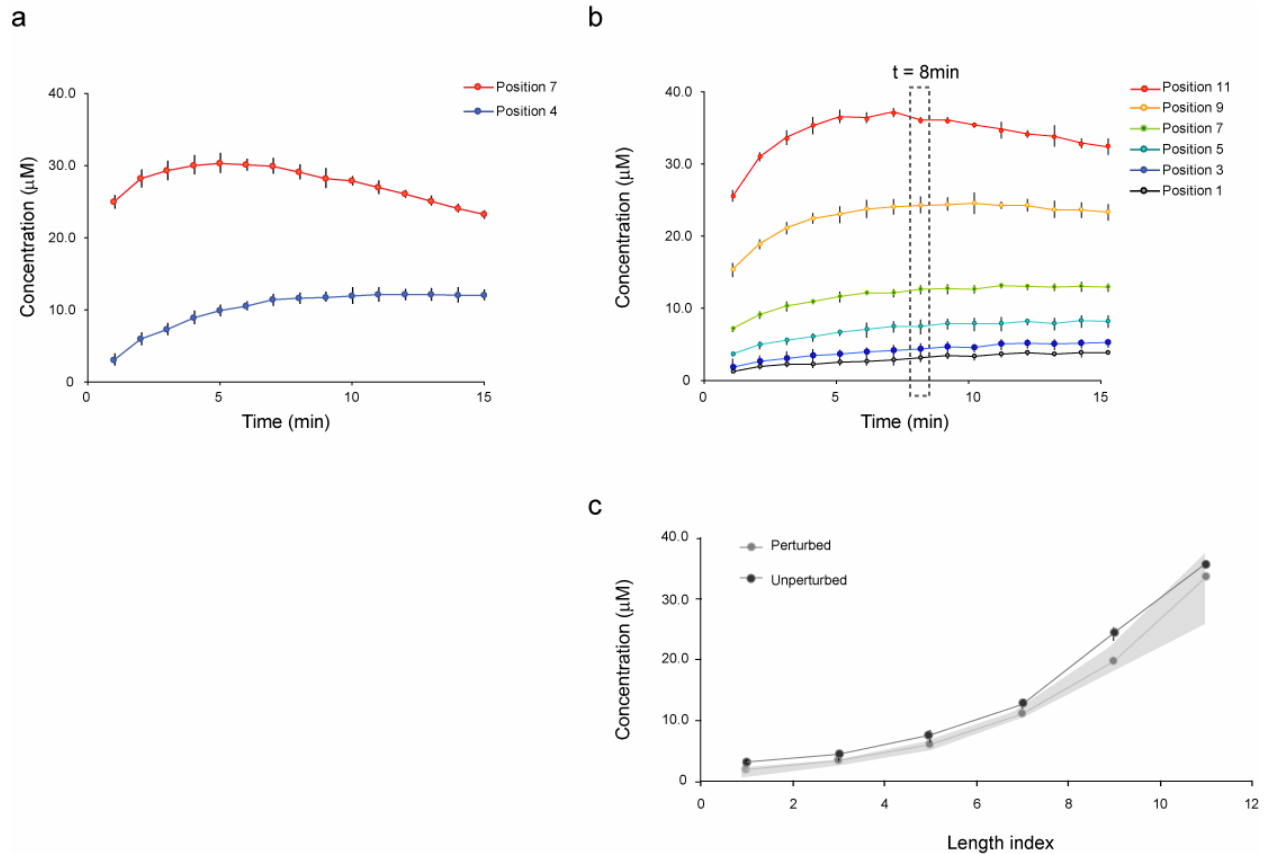
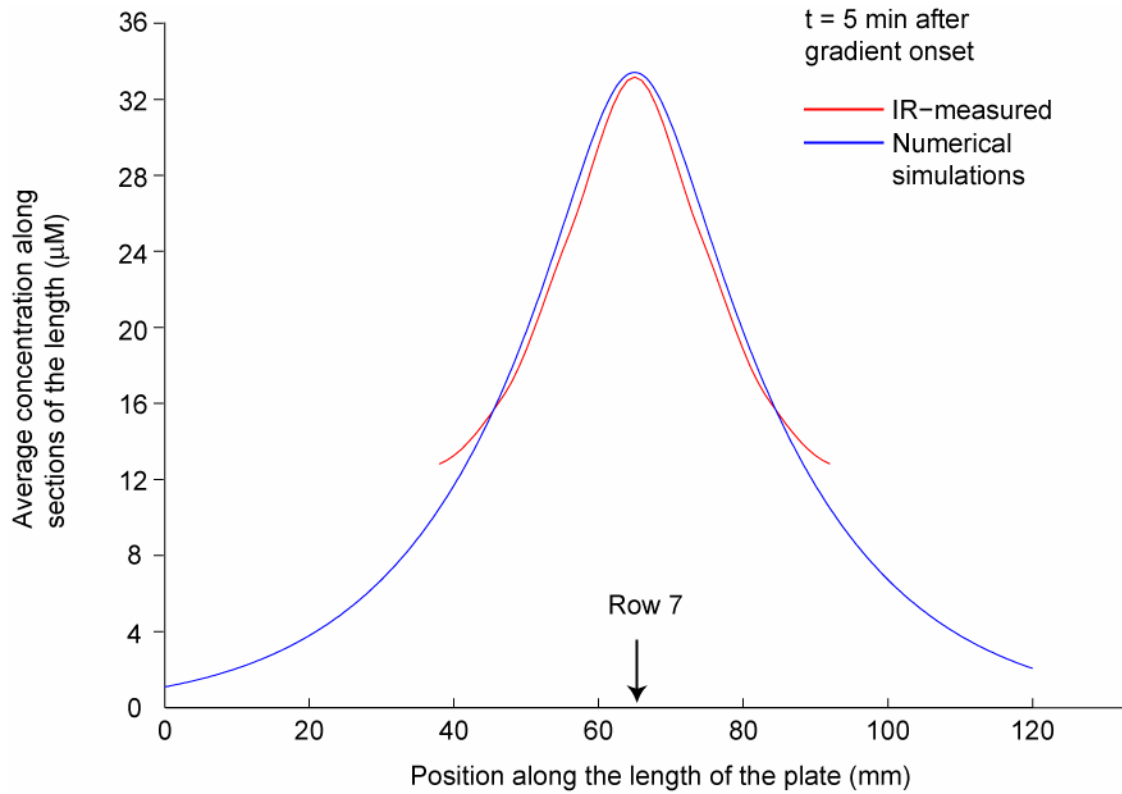**Supplementary Figure 4: Odor concentration time courses at different positions of the plate assay.** **(a)** Control of the isoamyl acetate dilution series used to create a HIGH amplitude exponential gradient (**Fig. 1b**). The positions corresponding to each concentration are shown in red on the top of the graph: E2: 0.03 M, E4: 0.06 M, E6: 0.12 M, E8: 0.25 M, E10: 0.50 M and E12: 1.00 M. The absorbance corresponding to the 6 dilutions (solvent: paraffin oil) was measured by IR spectroscopy in liquid phase using a standard flow cell (wavenumber: 1750 cm^{-1}). The alignment of the data points demonstrates the excellent agreement between theoretical and actual concentrations. **(b)** Time courses of the isoamyl acetate concentration in gaseous phase across rows 1 to 12. The concentrations were calculated from the absorbance measured at wavenumber 1764 cm^{-1}. The initial odor loading is given in **Supplementary Fig. 4a**. From these time courses at fixed positions, we determined the length profiles. For instance, the profile along the length of the plate at t = 8 min (**Fig. 1d**) was reconstructed from the concentrations contained in the dashed gray box.
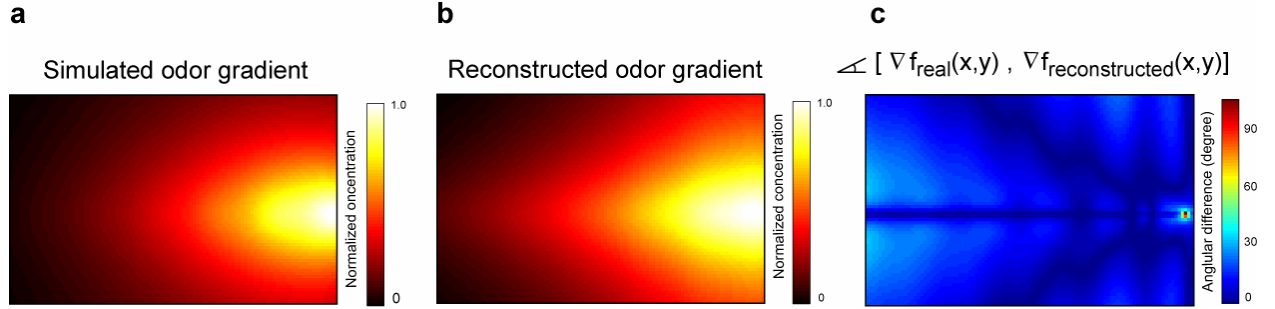
Supplementary Figure 5: Inter-trial reproducibility and persistence of the gradient upon perturbations. (a) Time courses of average odor concentrations measured along rows 4 and 7 for the single-odor-source assay (**Fig. 1a**). The source concentration was isoamyl acetate 1.00 M. Mean concentrations were calculated from three independent measurements at each position. Standard deviations are reported as error bars. **(b)** Time course of the average odor concentration measured along rows 1, 3, 5, 7, 9 and 11 for the multiple-odor-source assay (**Fig. 1b**). The gradients tested were of isoamyl acetate with HIGH amplitude exponential shape (source concentrations ranging between 0.03 and 1.00 M). **(c)** Perturbed profile reconstructed from concentration time courses measured along rows 1, 3, 5, 7, 9 and 11. The gradients tested were of isoamyl acetate with HIGH amplitude exponential shape. Every 3 minutes the top lid was removed for ~3 seconds. The length profile reconstructed from the perturbed recordings is shown in light gray whereas the unperturbed profile reconstituted from **(b)** at t = 8 min is shown in dark gray. We conclude that the gradient is not seriously affected by the perturbations necessary to introduce and replace individual larvae.

Supplementary Figure 6: Comparison of the IR–measured and numerically simulated average concentration profiles. Numerical simulations were carried out for a point source positioned at E7 and with a diffusion coefficient $D = 0.025$ cm^2 s^{-1}. The row where the source was positioned is indicated by an arrow. In the simulations, only positions located on the bottom surface of the plate assay were considered to compute the average concentration along sections of the length of the plate.

a

Simulated odor gradient

b

Reconstructed odor gradient

c

$\measuredangle \, [\, \nabla f_{real}(x,y) \, , \, \nabla f_{reconstructed}(x,y)\,]$

Supplementary Figure 7: Control of the reconstructed odorant gradients. (a) Simulation of the diffusion problem presented in **Fig. 1b** based on the numerical integration of equations (1)-(2). An exponential gradient is generated from the diffusion of 6 droplets with concentrations ranging between 0.03 and 1.00 M (**Fig. 1b** and **Supplementary Fig. 4a**). Concentrations were normalized to range between 0 and 1. **(b)** Gradient reconstructed from the cumulative profiles measured on the simulated gradient **(a)** and by applying equation (3). **(c)** Absolute value of the angle comprised between the direction of steepest concentration change measured on the real and the reconstructed gradients. Except for a localized singularity observed at the peak of the gradient (E12), we concluded that the gradient field was faithfully reconstructed.

Supplementary Figure 8: Characterization of speed and turning rate variations during chemotaxis behavior. (a) Analysis of the speed as a function of the absolute concentration for 100 trajectories of wild-type larvae tested in HIGH amplitude exponential gradients (multiple-odor-source assay, **Fig. 1b**). At every position, the instantaneous speed was measured over the previous 3 seconds. As in **Fig. 4a**, positions were grouped into 5 logarithmically equidistant zones of concentrations (contour lines) depicted in the bottom graph. Box plots represent the speed distribution found in each zone. The speed remained approximately constant throughout the gradient concentration range, except in the neighborhood of the gradient peak zone (concentrations > 51.5 μM) where a modest decrease was observed. **(b)** Analysis of the averaged turning rate as function of the speed for the data used in **(a)**. Turning rates were binned into 5 logarithmically equidistant groups of speeds (N = 100).
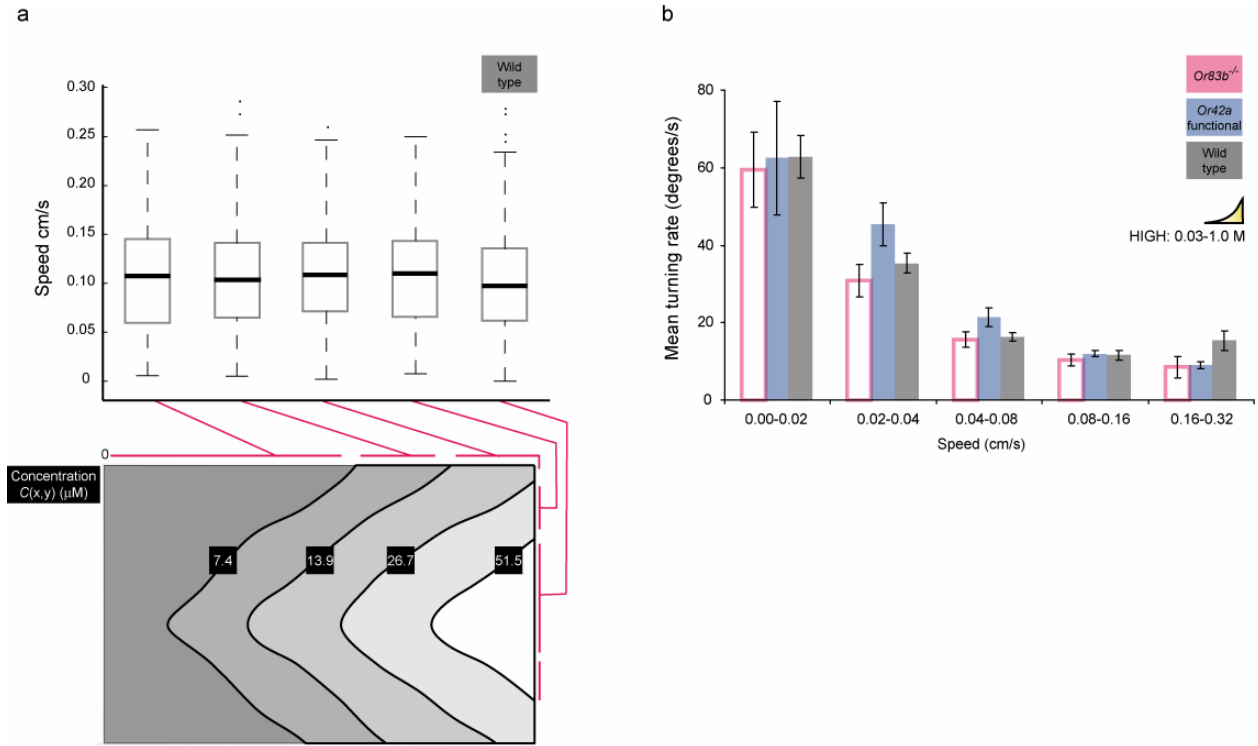
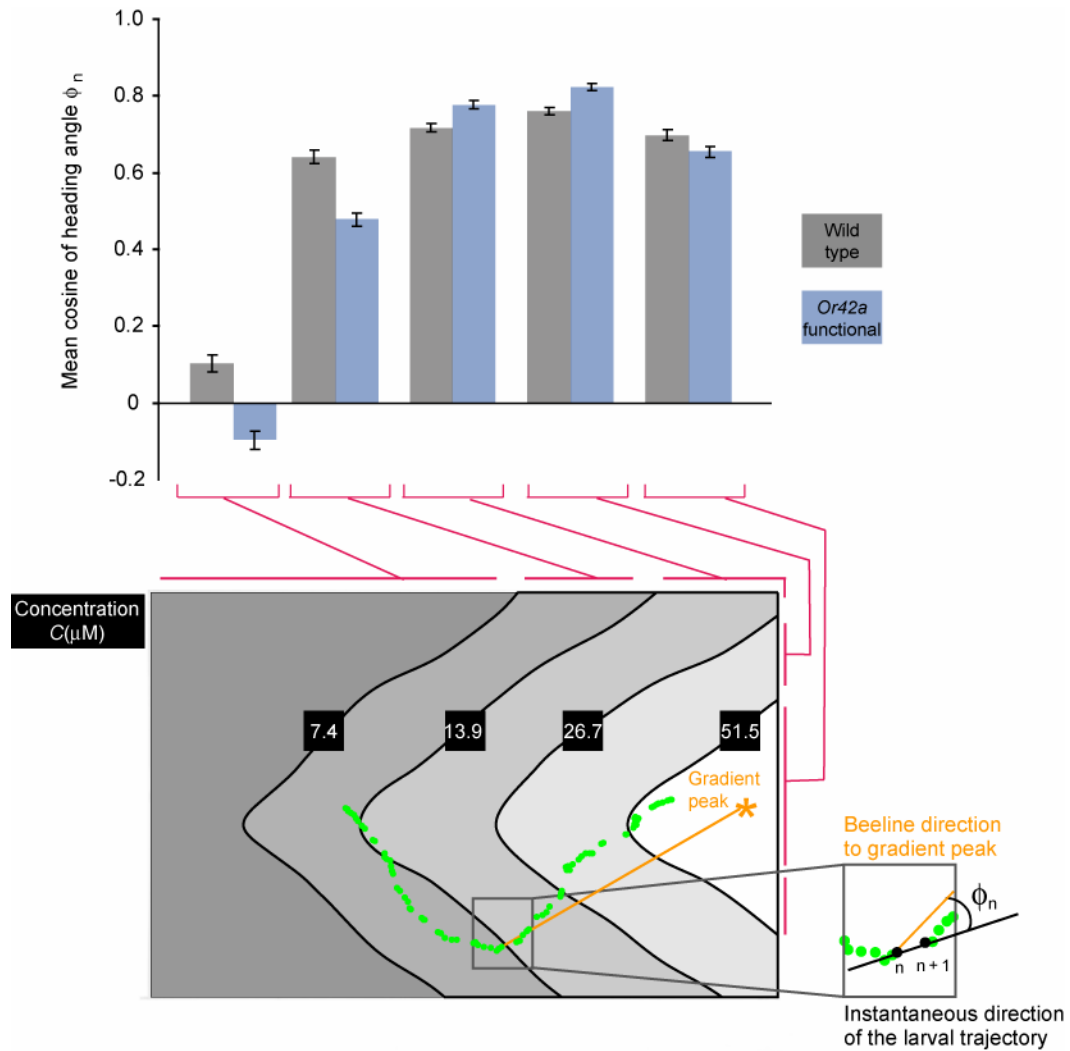**Supplementary Figure 9**: **Analysis of the instantaneous speed and turning rate as a function of the distance to the odor source (isoamyl acetate). (a)** Positions were grouped into 8 zones accordingly to their distance to the center of the odor source (denoted by a star). Consecutive zones are separated by 0.5 cm. **(b)** Instantaneous speed as a function of the distance to the source for $Or83b^{-/-}$ tested in the absence of odor (paraffin oil) or in the presence of 1.00 M of odor. **(c)** Same as **(b)** for wild-type larvae tested in the presence of very low odor concentration 0.06M (which corresponds to a condition below detection threshold for wild-type animals, see **Fig. 2c**), and for high odor concentration 1.00 M. Only positions in the first 4 zones are shown here because they account for more than 90% of data points. **(d)** Same as **(c)** for $Or42a$-functional larvae. Positions in the first 4 zones represent more than 95% of data points. **(e)-(g)** Mean turning rate as a function of the distance to the odor source for the same conditions as **(b)-(d)**. Error bars report 99% confidence intervals on (circular) means. N = 40 trajectories for all conditions.
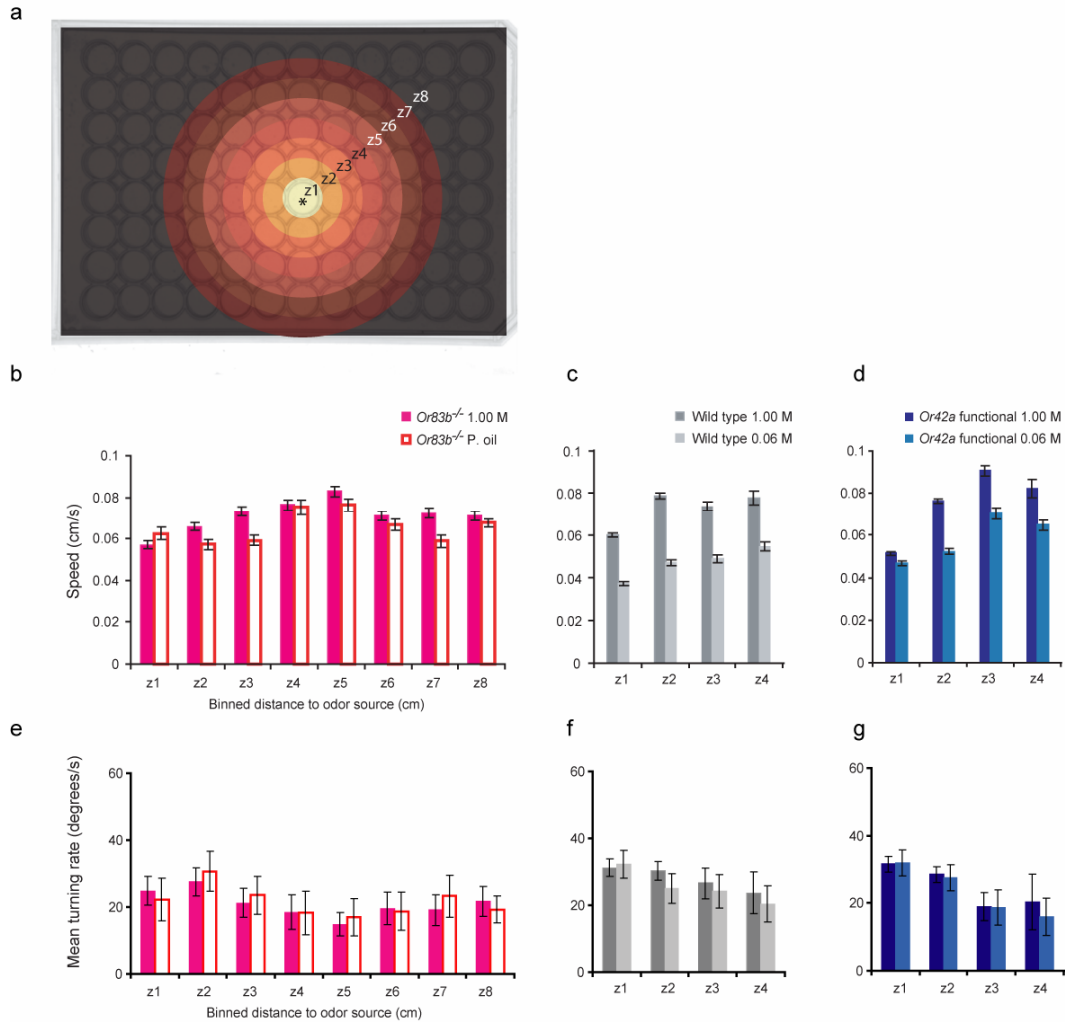
Supplementary Figure 10: Turning characteristics of larval chemotaxis. **(a)** Mean turning rate as a function of the absolute odor concentration. Mean and 99% confidence interval of distributions corresponding to different concentration zones are represented for three genotypes tested in HIGH exponential gradient of isoamyl acetate (N = 100). Turning rate distributions were compared between different concentration zones by applying a non-parametric Watson-Wheeler test (ref. [1]). The significance of these comparisons was assessed with a Bonferroni correction for 10 multiple tests (corrected P < 0.005). Samples labeled with different letters are statistically different. **(b)** Turning angle analysis of the trajectories of $Or83b^{-/-}$ mutant, $Or42a$-functional and wild-type larvae tested in the same conditions as **(a)** without grouping of position according to concentration zones. The mean turning angles were reported with 99% confidence intervals. No genotypes were found to have a turning angle distribution distinct from zero (ref. [1]). Angles were measured according to the counterclockwise convention. **(c)** Percentage of left (counterclockwise) and right (clockwise) turns for the same data as **(b)**.
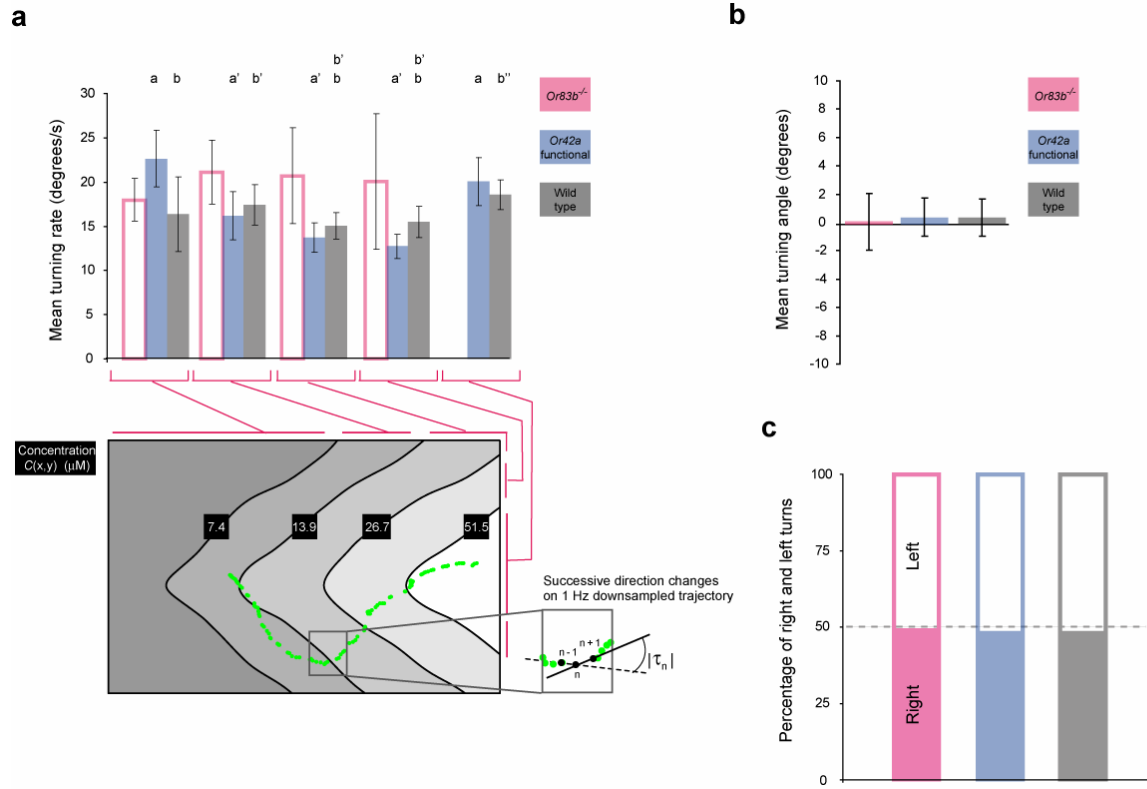
Supplementary Figure 11: Local heading angles measured with respect to the peak of the gradient for HIGH amplitude exponential gradient of isoamyl acetate. The peak of the gradient is indicated as an orange star. A heading angle ϕ_n was associated to every position of a given trajectory; positions were grouped into 5 logarithmically equidistant zones of concentrations (contour lines). Heading angles were weighted by a cosine function. The mean and standard deviation of the $\cos(\phi_n)$ corresponding to each concentration zones is reported as bar graph for trajectories of wild-type and *Or42a*-functional larvae (N = 100).

a

Downsampled trajectory (1 position/sec)

Distance to middle of row E

d_n

Direction pointing to the gradient peak (*)

Instantaneous direction of the larval trajectory

ϕ_n

n

n + 1

b

f(ϕ_n) Heading score

ϕ_n Heading angle with respect to the gradient peak (*)

c

g(d_n) Distance score

d_n

B C D E F G H
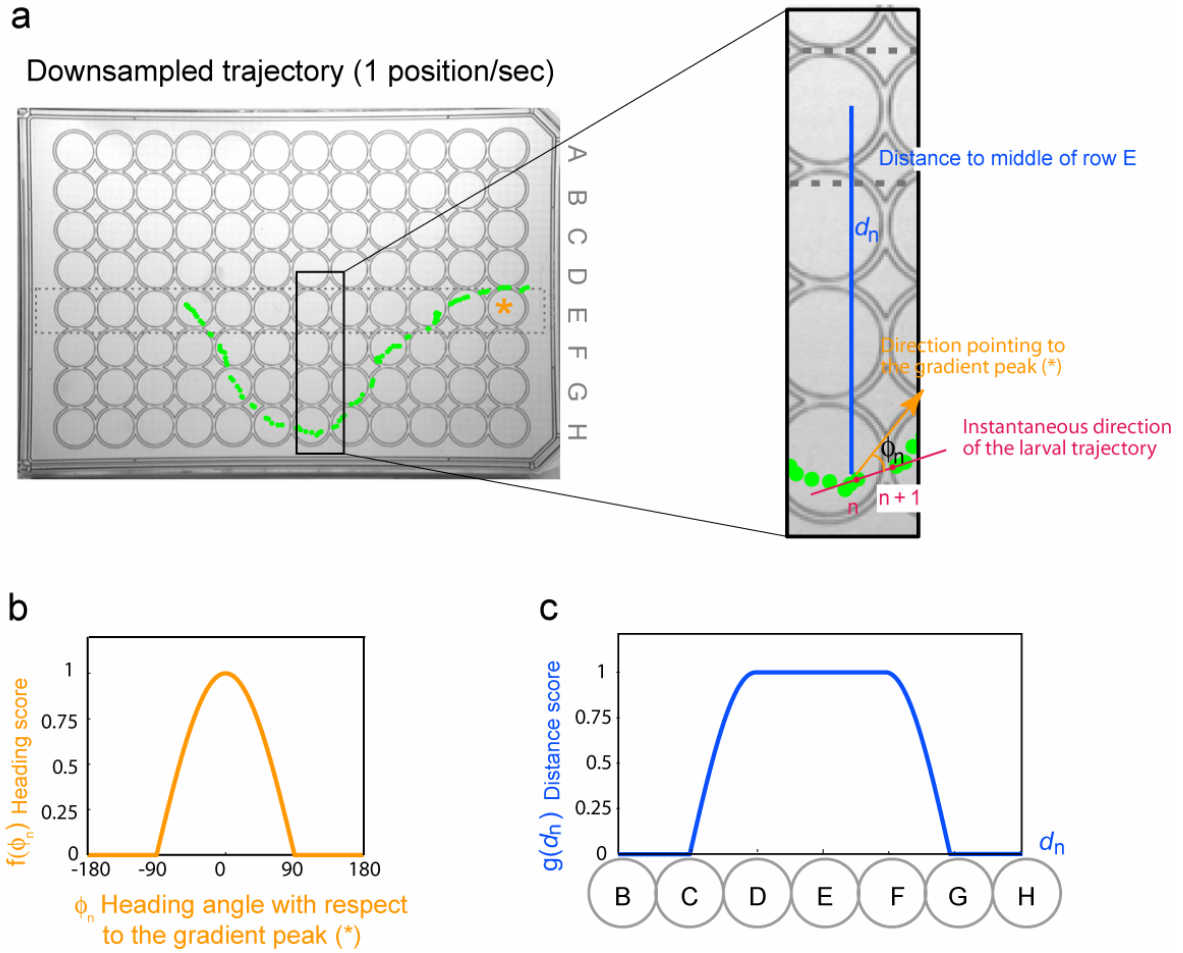
Supplementary Figure 12: Combined chemotaxis score. (a) Raw trajectories recorded at a rate of 6Hz were first downsampled to 1Hz as explained in the text. The peak of the gradient is represented by an orange star (*) in the plate. At each position (x_n,y_n) of the downsampled trajectory, the instantaneous direction of the animal's motion was determined. This direction was given by the axis connecting positions (x_n,y_n) and (x_{n+1},y_{n+1}) (red line in right inset). In addition, the angle ϕ_n comprised between the instantaneous direction of motion and the direction pointing toward the peak of the gradient (orange arrow) was computed. The beeline distance d_n between the position (x_n,y_n) and the center of the odor line was computed. **(b)** Heading score function for the angle ϕ_n. **(c)** Distance score function to weight d_n.

Supplementary Figure 13: Illustration of the side-dependent turning bias analysis on fictive trajectory. All analyses were performed on downsampled trajectories re-discretized to keep the step size similar between consecutive positions (~0.5 cm). The side-dependent turning angle was defined as the angle comprised between the instantaneous directions of motion of three successive positions. This angle was measured between -180 and +180 degrees; the sign of the angle was corrected based on the direction of the previous step. Turns correcting the previous step, or orientation, toward the local odorant gradient (blue vector field) were measured positively ($\tau 3$ and $\tau 10$–green) whereas those pointing away from the local gradient were measured negatively ($\tau 6$–red). For details, see ref. [2].
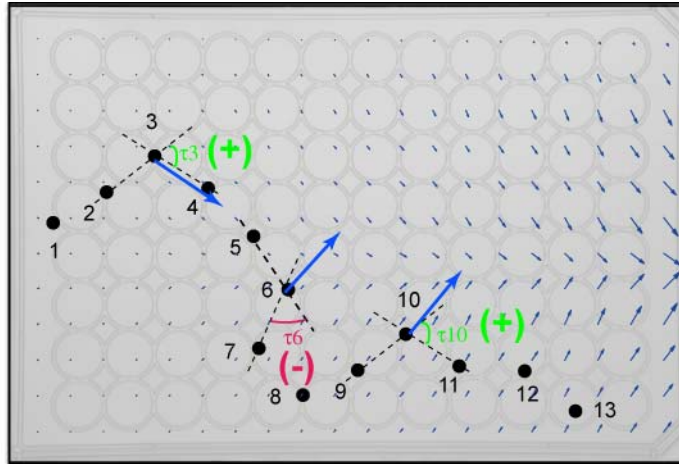
Supplementary Figure 14: Turning characteristics of unilateral and bilateral *Or42a*-functional rescues. **(a)** Averaged turning rate as a function of the absolute odor concentration. The mean and 99% confidence interval of turning rate distributions corresponding to different concentration zones are represented for *Or83b*$^{-/-}$, unilateral left, right, and bilateral rescues. All individuals were tested in HIGH exponential gradient of isoamyl acetate (N = 100). **(b)** Analysis of turning angles as a function of the absolute odor concentration (means and 99% confidence intervals) for the same data and concentration zones as **(a)**. **(c)** Mean turning angle and 99% confidence interval computed on all pooled positions. No genotypes have a non-zero turning angle distribution (ref. [1]). All angles were measured according to the counterclockwise convention. **(d)** Percentage of left (counterclockwise) and right (clockwise) turns.
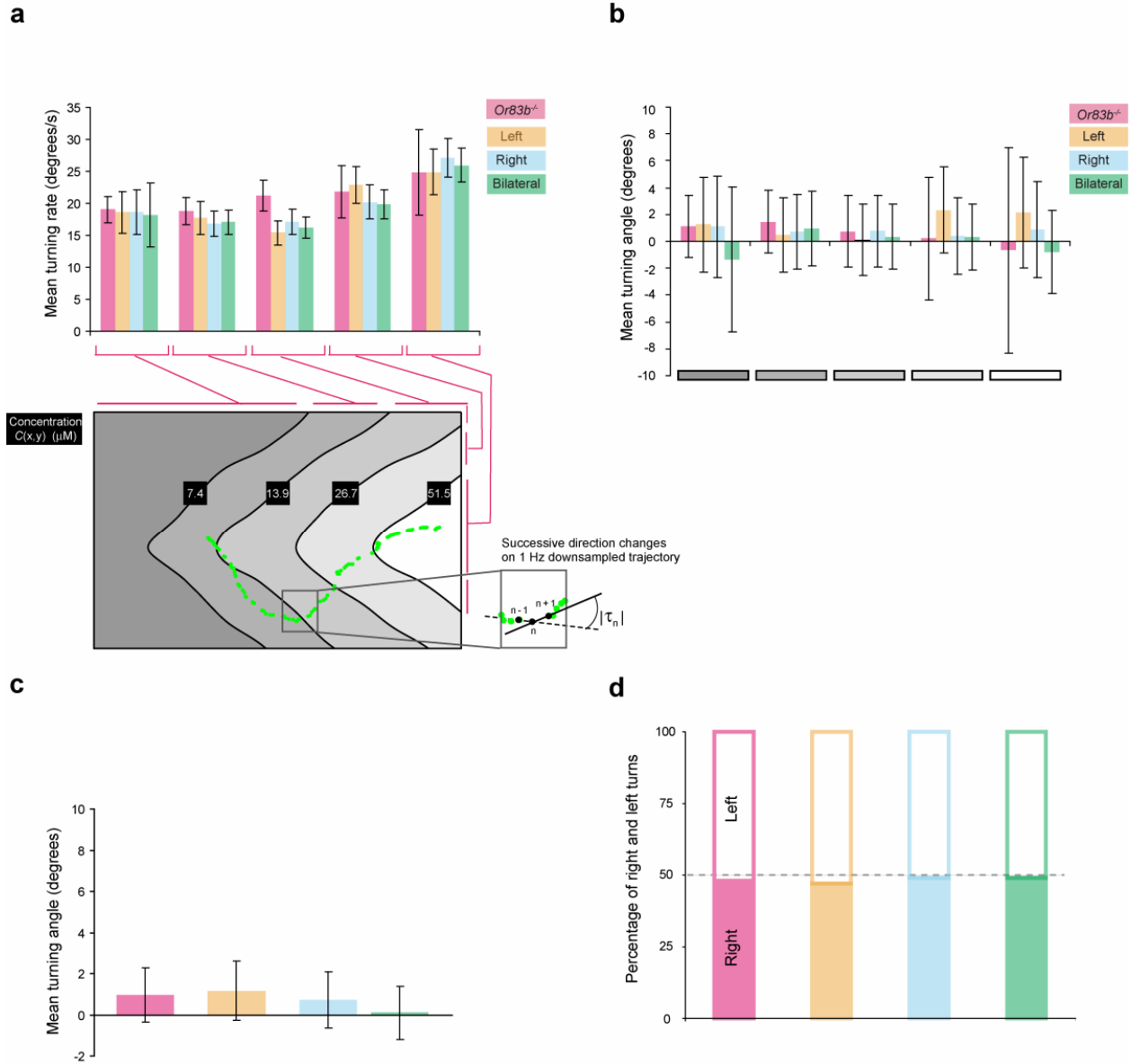
Supplementary Figure 15: Effect of gradient reversal and heat-shock treatment. (a) Analysis of combined chemotaxis score measured for left and right unilaterally rescued larvae tested for HIGH amplitude exponential gradients set up along row D (left) and row E (right). Due to the presence of an even number of rows in the 96-well plate lid, the odor distribution was slightly skewed toward the North or the South of the plate depending along which row the odor line was set. Whereas unilateral right behave significantly better than unilateral left rescues for gradients set up along row E (Wilcoxon test, $P < 0.003$), the opposite effect is not observed for gradients set up along row D (Wilcoxon test, $P = 0.5$). **(b)** Analysis of combined chemotaxis score measured for unilateral rescues (left and right combined) subjected or not to a 15 min. heat-shock (HS) treatment. The absence of differences between the medians (Wilcoxon test, $P > 0.99$) demonstrates that short heat-shock treatment had no effect on larval chemotaxis. N = 100 for all conditions. Statistical results are presented as in **Fig. 2**.
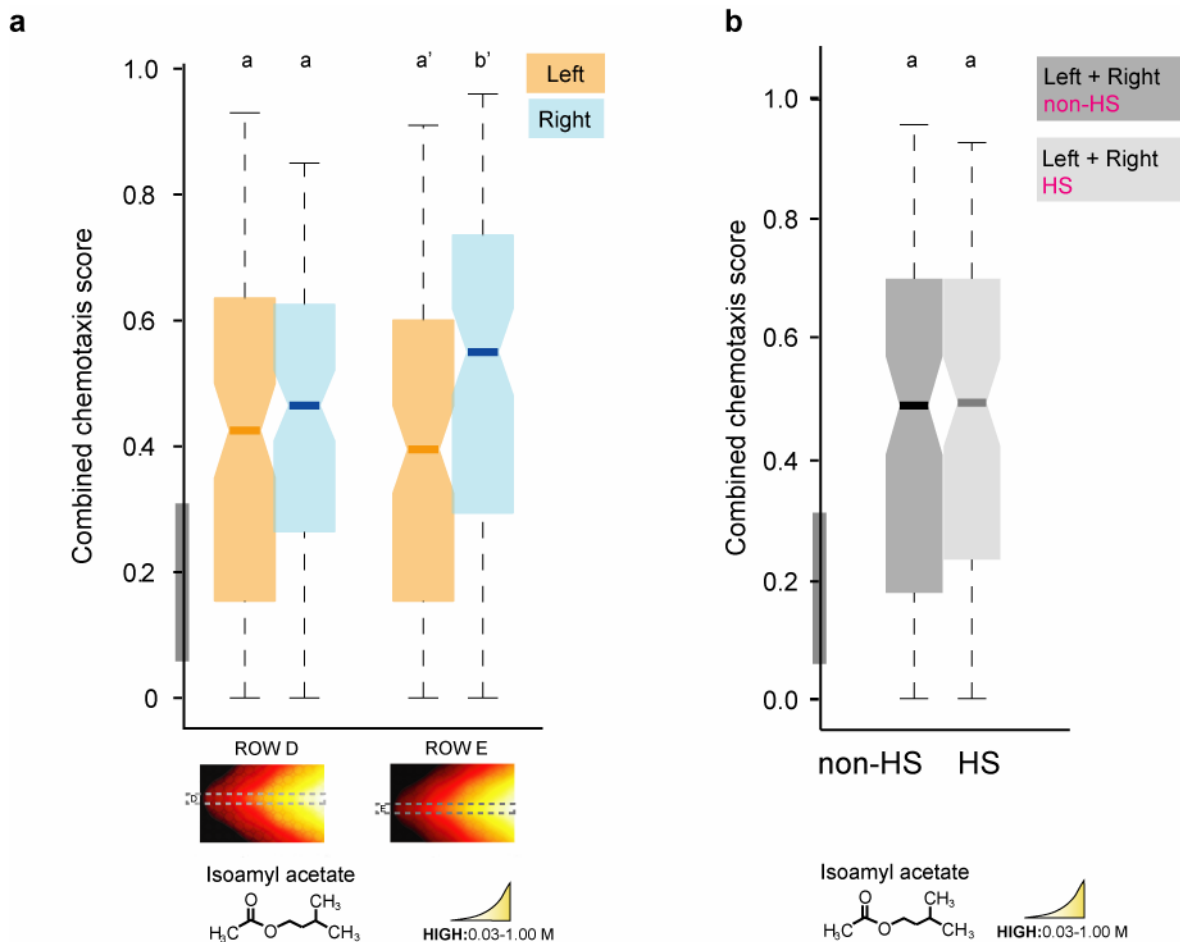
Supplementary Figure 16: Odorant gradients of differing shapes. (a) Length profiles of averaged concentration measured between 4 and 12 min after isoamyl acetate odor loading [HIGH exponential (yellow), steep linear (green) and shallow linear (blue)]. Variation around the mean concentration is indicated by the shaded background. **(b)** Width profiles of gradients in **(a)**.
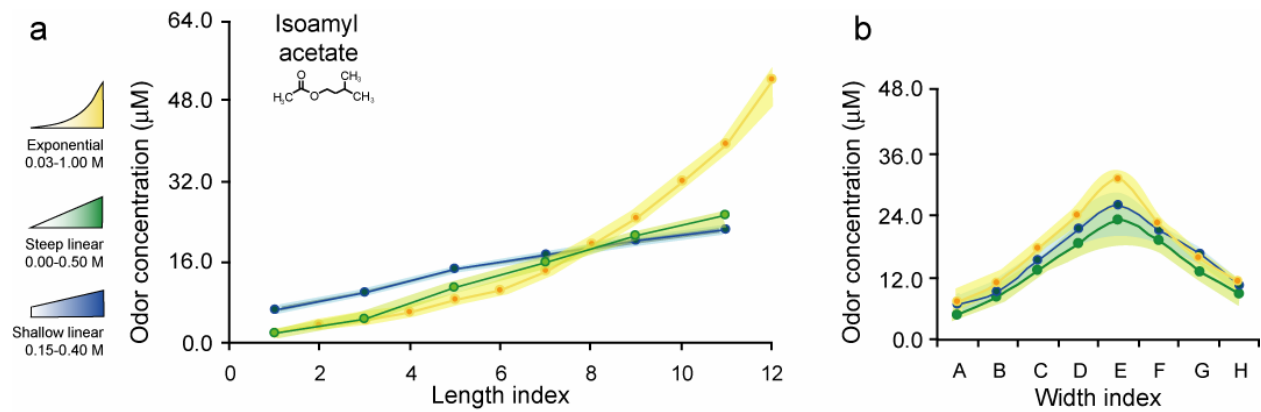
Supplementary Figure 17: Average concentration time courses recorded for the first minute of trajectories corresponding to unilateral and bilateral rescues tested for isoamyl acetate gradients. **(a)** HIGH amplitude exponential gradients. Mean concentrations are reported in as a plain line with the shaded background representing standard errors. For each time point, concentration averages were computed based all trajectory points used in **Fig. 5**. **(b)** Steep linear gradients (all data points used in **Fig. 8d-e**). **(c)** Shallow linear gradients (all data points used in **Fig. 8i-j**).
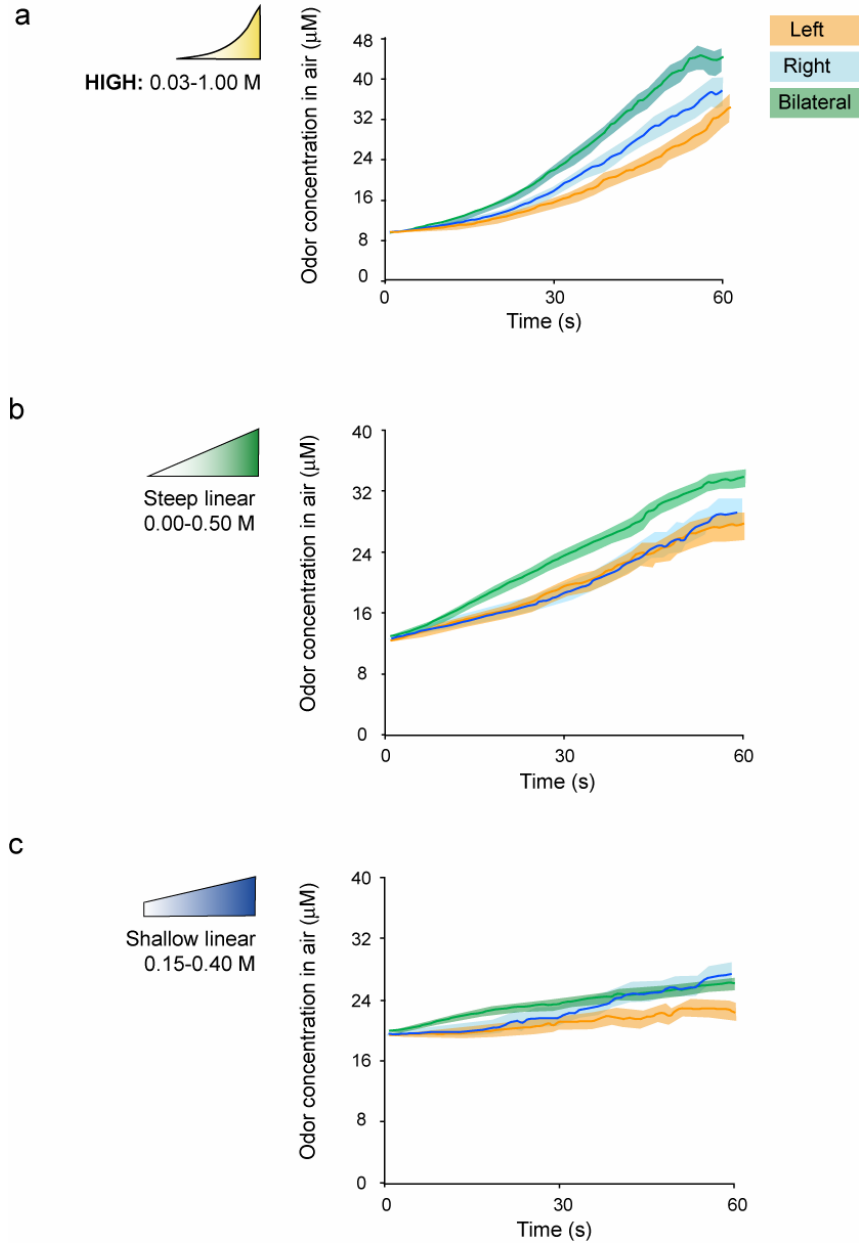
Supplementary Table 1: Concentration conversion for single-odor-source device

Source concentration (M)	Maximum concentration in air (μM) under the odor source
1.00	85
0.50	42
0.25	21
0.12	10
0.06	5
0.03	3

Odorant: isoamyl acetate

Supplementary Methods

Generation of Or83b FLP-out construct

Plasmid constructs were generated by amplification of the desired cDNA

fragments with flanking restriction sites by PCR. The Flipase (FLP)-out construct

comprises RFP cDNA[3] joined to the hsp70 transcription termination sequence. The

cassette is flanked by two FRT sites (denoted as '>') followed by the *Or83b* cDNA

tagged with GFP (*GFP:Or83b*)[4]. The GFP tag comprised full-length EGFP (Clontech,

Palo Alto, California, United States) lacking the STOP codon. The final construct

(UAS>*RFP*-stop>*GFP-Orb83b*) was cloned into pUAST[5] for transgenic expression.

Single- and multiple-odor-source devices

To create stable and controllable odor environments, we used the odor delivery

device described in **Supplementary Fig. 1a**, which comprises three 96-well plate lids

stacked on top of each other. The bottom lid was used to isolate the two other lids from

the supporting surface and to minimize heat convection in the behavioral assay. The

upper surface of the middle lid was evenly coated with 25 ml of 3% agarose dissolved in

distilled water, producing a thin (~3 mm), smooth, and moist surface suitable for

Drosophila larvae to crawl. The third plate was initially inverted and odors were

introduced into subsets of the 96 condensation rings imprinted in the concave interior

surface of the top lid. Odors (10 μl droplets) were dissolved in paraffin oil. For the

single-odor-source device, one odor droplet was placed in position E7. To create more

complex gradients along row E, the multiple-odor-source device was constructed by

placing six odor droplets of increasing concentrations in positions E2, E4, E6, E8, E10,

and E12. After introducing the odor droplets, the top lid was carefully inverted onto the

middle lid. The odor/oil droplets remained suspended by surface tension to the rings,

forming a "ceiling" overlying the agarose surface on the middle lid. One minute after the

odor was loaded in the top lid, and the top lid was inverted on the middle lid, individual

larvae were introduced onto the agarose surface of the middle lid at position E3–E4 and

their locomotor activity was tracked with a CCD camera. Larvae never contacted the oil

droplets hanging from the ceiling of the chamber. Images were acquired and processed

with Ethovision software (Noldus). Data were analyzed with Matlab (The MathWorks).

Measuring odorant gradients by infrared spectroscopy

We devised custom instrumentation that allowed us to insert these single-

/multiple-odor-source devices into a Nicolet Magna 560 Fourier transform-infrared (FT-

IR) spectrometer outfitted with a photoelectric detector (Mercury Cadmium Telluride A,

Thermo Electron Corporation, Madison, WI) and directly measure odor concentrations

in vapor phase. The three plate device described in **Supplementary Fig. 1a** was

enclosed in a custom aluminum box with sliding walls fabricated by The Rockefeller

University High Energy Physics Machine Shop (**Supplementary Fig. 1b**). Two inserts

of IR-transparent calcium fluoride (Sigma-Aldrich) were mounted into holes drilled into

both walls of the Plexiglas box (blue arrow in **Supplementary Fig. 1b**). This

configuration allowed access of the IR beam to the sample. Odor concentrations were

measured along transverse sections of the plate by inserting the whole apparatus into

an IR spectrophotometer. The IR beam of the spectrophotometer was focused through

the calcium fluoride windows into the side of top lid, lengthwise or widthwise, with the

beam approximately centered in the vertical direction (see schematic in **Supplementary**

20

Fig. 2). Absorbance spectra were computed by a Fast Fourier Transformation algorithm (OMNIC software, Thermo Scientific). To reduce noise, absorption spectra were calculated from multiple scans (90–100 scans). We were therefore limited to an overall sampling rate of one per minute.

Our absorbance measurements required us to remove any IR-blocking polystyrene along the IR beam path. This was achieved by cutting out two small windows from the side walls and repetitively measuring the absorbance at a given position (**Supplementary Fig. 2**). This solution offered the advantage of minimizing odor loss but required a new plate for each position probed. Due to practical constraints imposed by IR-spectroscopy, odor concentration could not be measured directly in parallel with the behavioral experiments.

Converting odor absorbance to odor concentration

Absorbances were measured at wavelengths that did not overlap with the absorption spectrum of water and CO_2 (e.g. 1750 cm^{-1} for isoamyl acetate). They were converted into absolute concentrations based on the Beer-Lambert law

$$c = \frac{A}{\varepsilon \times l}$$

where l is the length of the path followed by the beam in the odor sample and ε the molar extinction coefficient. For the four odor molecules used to create odorant gradients and to measure resulting profiles (**Fig. 1, 3-5, 8**), we determined ε empirically in gaseous phase by using a standard demountable gas cell filled with an airborne odor of known concentration. The gas cell (Sigma-Aldrich) had a cylinder shape with diameter 2.8 cm and length 10.2 cm (IR beam path length). Absorbance was measured across the gas cell length upon injection of a small volume of odor. To minimize errors

in odor sample concentrations, we used solutions of pure odor mixed with hexane at a dilution factor of 1/5, 1/10 and 1/20. We injected 5 μL of these solutions directly in the gas cell, which corresponded to a volume of pure odor of 0.25 μL, 0.50 μL or 1.00 μL. For the wave numbers considered, we verified that hexane had a negligible contribution to the absorption of the gaseous mixture. Our measured absorbances and estimations of molar extinction coefficients are reported in **Supplementary Fig. 3a-d**.

Odorant gradients with different geometries were obtained by changing the dilution series used to fill the six droplets of the top lid (**Fig. 1b,d,f** and **8a,f**). For instance, a gradient with exponential shape was generated from a binary dilution series where E2: 0.03 M, E4: 0.06 M, E6: 0.12 M, E8: 0.25 M, E10: 0.50 M and E12: 1.00 M. Ratios between the concentrations of the dilutions series were controlled in liquid phase using a flow cell (**Supplementary Fig. 4a**).

The time course of the average concentrations along rows 1 to 12 is shown in **Supplementary Fig. 4b**. From these data, we reconstructed the concentration profile along the length of the plate at different times (e.g. **Fig. 1c** and **1d**). Interestingly, we notice that while the positions corresponding to the high concentration droplets (E10–12) decrease in concentration over time, the positions corresponding to the low concentration droplets (E2–4) tend to increase in concentration. This phenomenon can be explained by the diffusion of odor molecules from the region of higher concentrations to the region of lower concentrations.

In **Supplementary Fig. 4b**, all concentration time courses corresponding to different positions were obtained for different lids and therefore represented distinct experiments. To measure the inter-trial variability of gradients created in the single- and

multiple-odor-source assays, we performed three independent measurements of the time course at several positions. The mean and standard deviation of the concentrations obtained for a given time point are shown in **Supplementary Fig. 5a,b**. Our results establish the excellent inter-trial reproducibility of our gradients.

The time courses presented in **Fig. 1c** and **1d** were obtained for unperturbed conditions where the top lid was not moved during the course of the recording. Yet perturbations could not be avoided during our behavioral experiments as individual larvae were introduced in the plate assay by lifting the top lid. We thus asked whether successive openings of the lid affected the geometry and amplitude of the odorant gradient field. We created HIGH amplitude exponential gradient of isoamyl acetate and mimicked animal replacements by removing the top lid every 3 minutes for ~3 seconds.

The concentration time courses were measured along rows 1, 3, 5, 7, 9 and 11. Length profiles corresponding to different time points were reconstructed and compared to the profiles generated in the absence of perturbations (**Supplementary Fig. 5c**). There is a small decrease in the absolute concentration between the perturbed and unperturbed profiles, but this is expected to be systematic across experiments. We conclude that the gradient is remarkably stable, even when perturbed by intermittent lid-openings.

Numerical simulation of odor diffusion

The IR spectroscopy method described above permitted us to measure absolute average concentrations along sections of the width and length of the plate assay. To determine odor detection thresholds and study the local alignment of an animal's trajectory with the odorant gradient, we needed to estimate the gradient vector field at

~N^2 positions from the average concentrations measured at ~2N positions. This 'tomography' problem has no unique solution. It was resolved by taking advantage of numerical simulations.

To reconstruct the odorant gradient generated in the single-odor-source assay (**Fig. 1e**), we simulated the establishment of the odorant gradient computationally. Taking the geometry of the plate assay into account, we modeled the release of odor from the oil droplets as a simple diffusion process arising from a set of point sources. Since the plate assay is not sealed, it is reasonable to assume in a first approximation that the walls are non-existent. Furthermore, we made the assumption that the oil droplets represent constant source terms and that odor exchanges between the air and the agarose layer can be neglected. Supposing that diffusion starts at time t = 0 and considering the contribution of a single droplet located at position (x_s, y_s, z_s), the odor concentration C at time T and point (x,y,z) is [6]:

$$C(x, y, z, T) = \int_0^T \frac{J}{(4\pi D t)^{3/2}} e^{-r^2/(4 D t)} dt \tag{1}$$

where $r = \sqrt{(x - x_s)^2 + (y - y_s)^2 + (z - z_s)^2}$ and J represents the odor out-flux from the droplet. In our simulations, we fixed $(z - z_s)$ equal to 1 cm. For the odorant molecules used in our study, the typical value of the diffusion coefficient is in the order of 0.01–0.10 cm^2 s^{-1} (see for instance reference [7]). At any position of the device, we assumed that the concentration resulting from the diffusion of the N droplets is given by the sum of the individual contributions. This is physically justified by the fact that all diffusion processes occur independently:

$$C^{\text{total}}(x, y, z, T) = \sum_{i=1}^{N} C_i(x, y, z, T) \tag{2}$$

Reconstruction of odorant gradient found in single-odor-source assay

In **Fig. 1c**, we reported the average odor concentrations measured by FT–IR spectroscopy along different sections of the plate assay. This information was used to estimate the odor concentration in every position of the plate. For a 1.00 M source of isoamyl acetate, we numerically simulated the diffusion process taking place in the plate upon odor release from the source. We adjusted the diffusion coefficient of equation (1) to obtain a good fit between the average concentration profile generated by numerical simulations and those observed by IR-spectroscopy (**Supplementary Fig. 6**). Five minutes after gradient onset, the best fit was obtained for a diffusion coefficient of 0.025 $cm^2 s^{-1}$. This value is remarkably close to that found in the Handbook of Chemical Property Estimation Methods [7] for isoamyl acetate (0.067 $cm^2 s^{-1}$). The simulated gradient shown in **Fig. 1e** was obtained 5 min after the beginning of the odor release.

Based on our numerical simulations, we estimated the odor concentration in air found under the source for different odor loadings. For a 1.00 M source of isoamyl acetate, the resulting concentration in air is 85 μM (t = 5 min after gradient onset). Assuming that the shape of the odorant gradients resulting from different source concentrations is qualitatively similar and simply rescaled, we generated the conversion in **Supplementary Table 1**.

Reconstruction of odorant gradient found in multiple-odor-source assay

For the multiple-odor-source assay, we combined the information contained in the length and width concentration profiles (**Fig. 1d**). We assumed that the geometry of

the cumulative profile along the width did not significantly deviate from any actual width profiles along the width of the plate. Accordingly, we approximated the two-dimensional concentration function by

$$c(x, y) \cong c \times v(x) \times w(y)$$.

Further approximation in terms of discrete functions gives

$$c_{i,j} = c \times v_i \times w_j$$

with

$$v_i = v(i \times \Delta_x)$$

and

$$w_j = w(j \times \Delta_y)$$

The index ranges are

$$i = 1, 2, ..., M$$

and

$$j = 1, 2, ..., N$$

For the 96-well plate odor-source devices (**Supplementary Fig. 2**),

$$M = 8$$

and

$$N = 12$$

The cell size is equal in both dimensions

$$\Delta_x = \Delta_y = 0.9 \text{ cm}$$

Normalization of the functions v and w

$$\sum_{i=1}^{M} v_i = 1$$

$$\sum_{j=1}^{N} w_j = 1$$

yields

$$c \times w_j = \sum_{i=1}^{M} c \times v_i \times w_j = \sum_{i=1}^{M} c_{i,j}$$,

$$c \times v_i = \sum_{j=1}^{N} c \times v_i \times w_j = \sum_{j=1}^{N} c_{i,j} \qquad ,$$

and

$$c = \sum_{i=1}^{M} \sum_{j=1}^{N} c \times v_i \times w_j = \sum_{i=1}^{M} \sum_{j=1}^{N} c_{i,j}$$

The observable absorbances along the rows and columns are

$$A_j = \varepsilon \times \Delta_x \times \sum_{i=1}^{M} c_{i,j} = \varepsilon \times \Delta_x \times c \times w_j$$

and

$$A_i = \varepsilon \times \Delta_y \times \sum_{j=1}^{N} c_{i,j} = \varepsilon \times \Delta_y \times c \times v_i$$

It finally follows that

$$c_{i,j} = \frac{A_i \times A_j}{\varepsilon \times \Delta_x \times \sum_{i=1}^{M} A_i} = \frac{A_i \times A_j}{\varepsilon \times \Delta_y \times \sum_{j=1}^{N} A_j} \qquad (3)$$

Equation (3) was used to convert absorbances into odor concentrations in vapor phase.

In **Fig. 1**, **4**, **5**, and **8**, the odorant gradients were reconstructed from the cumulative

profiles obtained by IR-spectroscopy by averaging the absorbances measured between

4 and 12 min after the establishment of the gradient. In **Supplementary Fig. 7,** we

provide numerical evidence that the reconstruction lead to good results. Since we did

not have access to the two-dimensional odor distribution of any real gradient, we

simulated one based on equations (1)–(2) and the spatial characteristics of the plate

assay. We create an *in silico* exponential gradient with six virtual sources whose

concentration followed the geometrical series outlined in **Supplementary Fig. 4a**. In

Supplementary Fig. 7c, we compared the differences between simulated and

reconstructed gradient fields, and concluded that the reconstruction is faithful. This test

validated the use of the reconstructed gradient fields to analyze the correlation between larval heading and the direction of the local odorant gradient.

In the course of our study, we generated different types of isoamyl acetate gradients: one type with exponential shape and two with linear shapes (steep and shallow slopes). The three types of gradients were designed to have approximately the same total quantity of odor. The amplitude ranges of the two linear gradients were thus chosen so that their average concentration across the plate was similar to that of the HIGH amplitude exponential gradient. Based on the average concentration profiles shown in **Fig. 1d**, we calculated that the average odor concentration of the HIGH amplitude exponential gradient was $C^{exp} = 19 \ \mu M$. We constructed two linear gradients having an average concentration comprised between 15 and 20 μM and a slope significantly different along the length of the plate (**Fig. 8a** and **8f**, **Supplementary Fig. 16**).

Steep: E2 = 0.00 M; E4 = 0.10 M; E6 = 0.20 M; E8 = 0.30 M; E10 = 0.40 M; E12 = 0.50 M with an average concentration $C^{steep} = 17 \ \mu M$.

Shallow: E2 = 0.15 M; E4 = 0.20 M; E6 = 0.25 M; E8 = 0.30 M; E10=0.35 M; E12=0.40 M with an average concentration $C^{shallow}$=18 μM.

Quantification of behavioral data

The locomotor activity of each larva was monitored with a CCD camera at a rate of 6 frames per second (6 Hz). Each trajectory was downsampled by calculating the center of mass of every group of 6 positions recorded during the same second. This sampling rate reduction from 6 Hz to 1 Hz offered a simple and efficient way to decrease the level of noise caused by 'jittering' effects. Since the typical speed of a

larva was varied between 0.05 and 0.15 cm s^{-1} (see **Supplementary Fig. 8a**), the amount of meaningful meandering occurring during a one second interval was neglected.

After downsampling, all the positions were considered by successive pairs, say (x_n,y_n) and (x_{n+1},y_{n+1}). For each pair of positions, the instantaneous direction of motion of the animal was defined by the axis connecting the points (x_t,y_t) and (x_{t+1},y_{t+1}). Instantaneous speed and turning rates were computed on this basis. In **Supplementary Fig. 8b**, the turning rate was analyzed as a function of the speed. We observe that the turning rate is inversely correlated with the speed of the animal. This finding suggests that larvae slow down while they execute a sharp turn. Several approaches were used to quantify the ability of larvae to chemotax in a given odorant condition. These are described in detail below:

Variation of speed and mean turning rate as a function of the distance to the odor source (single-odor-source assay): At every position of the downsampled trajectory, the instantaneous speed and turning angle were measured. These variables were then analyzed as a function of the distance to the odor source for wild-type, *Or42a*-functional, and *Or83b*$^{-/-}$ larvae (**Supplementary Fig. 9)**. Mean turning rates were computed based on circular statistics [1]. For *Or83b*$^{-/-}$ mutants, two source concentrations of were considered: pure paraffin oil (no odor), and the highest concentration tested (1.00 M). For wild-type and *Or42a*-functional larvae, the two representative source concentrations used were: 0.06 M (generating no significant response in wild type) and 1.00 M (inducing strong attraction in both wild-type and *Or42a*-functional larvae) (**Fig. 2a,c**). For the higher source concentration, we observe

29

that larvae accumulate under the source (**Fig. 2a**). This phenomenon is not due to a complete suppression of motion under the source but seems to result from continuous turns in the source vicinity. In agreement with the results of **Supplementary Fig. 8b,** we find that the turning rate tend to increase under the source whereas the speed decreases.

Variation of the mean turning rate as a function of the odor concentration (multiple-odor-source assay): As previously explained, we measured the instantaneous turning angle corresponding to every position of our downsampled trajectories. Positions were grouped in zones of logarithmically equidistant concentrations (**Supplementary Fig. 10a,** bottom**)**. We observe that the mean turning rates tend to moderately decrease as the concentration increase. In additions, we calculated the mean turning angle over all positions and counted the percentage of left (counterclockwise) and right (clockwise) turns (**Supplementary Fig. 10b-c)**. Our results show no evidence supporting the existence of a turning bias for any of the genotypes tested.

Local heading angle analysis with respect to local odorant gradient (multiple-odor-source assay): At every position of the downsampled trajectory, we measured the heading angle between the instantaneous direction of the motion of the larva and the direction of the gradient or steepest concentration change computed from the reconstructed odorant gradient field (blue arrow in the inset of **Fig. 4b**). This angle θ was locally measured with respect to the gradient direction.

All the heading angles θ_n computed for different positions of trajectories corresponding to the same experimental conditions (gradient and genotype) were

combined and weighted by a cosine function. The best chemotaxis performances we observed corresponded to wild-type and *Or42a*-functional larvae navigating in exponential gradients of isoamyl acetate (0.03–1.00 M, **Fig. 2b,e**). In these conditions, we found that the alignment of larvae with the local odorant gradient improved as the odor concentration increased (**Fig. 4a**). Visual inspection of several trajectories (e.g. **Fig. 2b**) also suggested that trajectories were generally well aligned with the "beeline" (shortest direct route) pointing to the peak of the gradient (orange star in **Supplementary Fig. 11**). We tested this observation by recomputing the local heading with respect to the peak of the gradient (denoted as ϕ). The cosine of the heading angle ϕ distribution measured for 100 trajectories of wild-type (and *Or42a*-functional) larvae chemotaxing in HIGH amplitude exponential gradient were represented in **Supplementary Fig. 11**. We concluded that trajectories did not significantly deviate from the beeline to the gradient peak for a wide range of concentrations.

Combined chemotaxis score (multiple-odor-source assay): We designed a combined chemotaxis score quantifying the overall alignment of a trajectory with the odorant gradient. In this aim, we combined the information about the local heading of an animal and the distance separating the animal from the middle of the odor line. We computed the heading angles with respect to the peak of the gradient for two reasons. First, we observed that larvae tended to follow the direction of the gradient peak more accurately than the direction of steepest concentration change (**Fig. 4a** and **Supplementary Fig. 11**). Second, the direction to the gradient peak was computable even in the absence of any information about the reconstructed odorant gradient field. Let us denote this angle as ϕ (measured between -180 and 180 degrees). For every

position (x_n, y_n) of a trajectory, we scored the corresponding heading angle ϕ_n with a modified cosine function $f(\phi_n)$ shown in **Supplementary Fig. 12b**:

$$f(\phi_n)=\begin{cases} \cos(\phi_n) & \text{for } -90<\phi_n<90 \text{ degrees} \\ 0 & \text{otherwise} \end{cases} \qquad (4)$$

In addition, we measured the distance d_n between position (x_n, y_n) and the middle of row E. This distance was introduced into a scoring function $g(d_n)$ described in **Supplementary Fig. 12c**. Positions that were more than two rows (e.g., two condensation ring diameters) apart from the center of the odorant line were penalized by a score 0. Distances comprised between one and two ring diameters obtained an increasing score that reaches its maximum value 1 for all positions separated by less than one ring diameter from the center of the odorant line. The characteristics of the distance scoring function were qualitatively based on the actual odor distribution along the width of the plate (**Fig. 1d**).

For each position, a combined score was computed by taking the product of the heading score $f(\phi_n)$ and the distance score $g(d_n)$. We defined the chemotaxis score of a trajectory as the average of its combined scores over all positions:

$$\text{Combined chemotaxis score}=\frac{1}{N_{\text{positions}}} \sum_{i=1}^{N_{\text{positions}}} f(\phi_n) \times g(d_n)$$

Side-dependent turning bias (multiple-odor-source assay): To distinguish between direct and indirect orientation strategies (i.e. *taxis* versus *kinesis*), we followed a statistical procedure proposed by Benhamou and Bovet [2,8]. At each position, we computed the side-dependent turning angle. This angle quantifies the change in direction between two successive positions of the trajectory (**Supplementary Fig. 13**).

As explained in ref. [2], this analysis was performed on re-discretized trajectory of similar step length. To avoid accidental gaps due to positions that could not be resolved by the tracking software, re-discretization was performed on the raw trajectory after piecewise polynomial interpolation of the missing positions. We chose a re-discretization step not smaller than half the longest recorded step as measured on the downsampled trajectories and set it to 0.5 cm. Turning angles were measured between −180 and +180 degrees; the sign of individual angle was determined based on the direction of the previous step with respect to the direction of the local odorant gradient (reconstructed vector field in **Fig. 1f** and **Supplementary Fig. 13**). Sign corrections [2] were performed as follows: turning angles were measured counterclockwise if the previous step pointed to the right of the gradient, and clockwise if the previous step pointed to the left of the gradient peak (for illustration, see **Supplementary Fig. 13**).

In case of a kinesis mechanism, the probability of turning towards or away from the odor stimulus was expected to be equal. In contrast, we expected that for a taxis mechanism the probability of turning towards the odor stimulus was higher than away from it. Consequently, the mean of the side-dependent turning angles was expected to be not significantly different from 0 in a kinesis mechanism while it ought to be significantly higher than 0 for a taxis mechanism. Applying this procedure to wild-type and *Or42a*-functional larvae, we showed that, for high amplitude exponential gradient, the side-dependent turning angle distribution had a mean significantly higher than 0 (**Fig. 4b**). In contrast, we found no significant bias for the *Or83b* null mutants tested in the same conditions. These results allowed us to conclude that *Drosophila* larvae are likely to chemotax according to a taxis strategy.

References

1.	Zar, H.J. *Biostatistical Analysis*, (Prentice Hall, Upper Saddle River, 1999).
2.	Benhamou, S. & Bovet, P. Distinguishing between elementary orientation mechanisms by means of path-analysis. *Animal Behaviour* **43**, 371-377 (1992).
3.	Campbell, R.E. et al. A monomeric red fluorescent protein. *Proc Natl Acad Sci U S A* **99**, 7877-7882 (2002).
4.	Benton, R., Sachse, S., Michnick, S.W. & Vosshall, L.B. Atypical membrane topology and heteromeric function of *Drosophila* odorant receptors *in vivo*. *PLoS Biol* **4**, e20 (2006).
5.	Brand, A.H. & Perrimon, N. Targeted gene expression as a means of altering cell fates and generating dominant phenotypes. *Development* **118**, 401-415 (1993).
6.	Berg, H.C. *Random Walks in Biology*, (Princeton University Press, 1993).
7.	Lyman, W.J., Rosenblatt, D.H. & Reehl, W.J. *Handbook of Chemical Property Estimation Methods: Environmental Behavior of Organic Compounds*, (American Chemical Society, 1982).
8.	Benhamou, S. Detecting an orientation component in animal paths when the preferred direction is individual-dependent. *Ecology* **87**, 518-528 (2006).